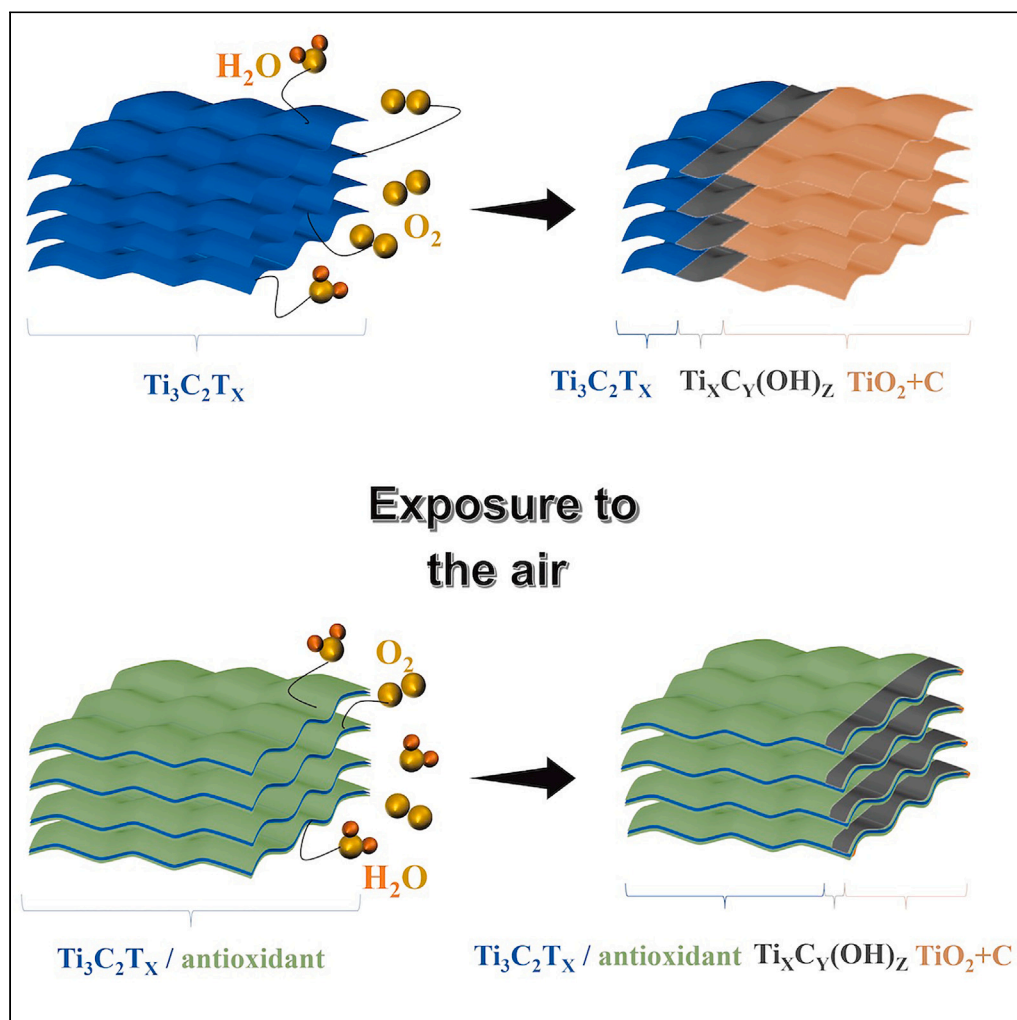Article

Robust Ti$_3$C$_2$T$_x$ MXene foam modified with natural antioxidants for long-term effective electromagnetic interference shielding

Guohong Wang,
Minghang Li,
Jianxi Liu, ...,
Xiaomeng Fan,
Xingmin Liu, Ralf
Riedel

jianxiliu@nwpu.edu.cn (J.L.)
liuxingmin19890101@126.com
(X.L.)

Highlights
Natural antioxidants were
employed to protect the
Ti$_3$C$_2$T$_x$ MXene from its
degradation

The effect of exposure
time in air of Ti$_3$C$_2$T$_x$/
antioxidant foam was
investigated

The EMI SE of Ti$_3$C$_2$T$_x$/TP
only decreased 4.6 dB

The antioxidation
mechanism of the applied
antioxidants is discussed

Article

Robust $Ti_3C_2T_x$ MXene foam modified with natural antioxidants for long-term effective electromagnetic interference shielding

Guohong Wang,[1] Minghang Li,[2] Jianxi Liu,[1,*] Fang Ye,[2] Laifei Cheng,[2] Xiaomeng Fan,[2] Xingmin Liu,[1,4,*] and Ralf Riedel[3]

SUMMARY

MXenes have been proven to be outstanding lossy phase of advanced electromagnetic interference (EMI) shielding materials. However, their poor tolerance to oxygen and water results in fast degradation of the pristine two-dimensional (2D) nanostructure and fading of the functional performance. Herein, in this research, natural antioxidants (e.g., melatonin, tea polyphenols, and phytic acid) were employed to protect the $Ti_3C_2T_x$ MXene from its degradation in order to achieve a long-term stability of the EMI shielding performance. The results showed that the synthesized composites comprised of antioxidants and $Ti_3C_2T_x$ exhibited a decelerating degradation rate resulting in an improved EMI shielding effective (SE) stability. The antioxidation mechanism of the applied antioxidants is discussed with respect to the nanostructure evolution of the $Ti_3C_2T_x$ MXene. This work contributes to the basic foundations for the further development of advanced MXenes for stable applications in the EM field.

INTRODUCTION

The fast proliferation of electronic devices and wide application of wireless communication technology have drastically increased the electromagnetic radiation (EMR) in our environment.[1–6] It was reported that EMR has become the fourth largest pollution source after noise, water, and air pollution and has adverse effects on the health of organisms (e.g., malfunctioning the central nervous system and causing sleep disorder).[7–9] To combat EMR, advanced electromagnetic interference (EMI) shielding materials that can effectively attenuate electromagnetic waves are becoming increasingly important.[10–17] As two-dimensional (2D) materials, MXenes have attracted great attention in EMI shielding fields due to their high electrical conductivity (higher than 10000 S/m), large specific surface area, and easy processability.[18–23] Its structural general formula is $M_{n+1}X_nT_x$, where M represents early transition metal (e.g., Ti, Zr, V, Nb, Ta, or Mo), X is carbon and/or nitrogen, and T_x is the terminating group (-OH, =O, and -F). $Ti_3C_2T_x$, as a representative member of MXene family, has been the most widely investigated. Both $Ti_3C_2T_x$ films[24–27] and foams[28–30] were reported to exhibit excellent EMI shielding effectiveness (EMI SE). However, due to the weak carbon-transition metal bonds resulting from the etching of main group (e.g., Al and Si) element(s), MXenes unavoidably exhibit poor stability and easy susceptibility even in air,[31] leading to a rapid decline in EMI shielding performance.

Many studies have been conducted to mitigate the oxidation behavior of $Ti_3C_2T_x$.[32] One possible route is to control the factors that influence the oxidation rate of the MXene flakes (e.g., temperature and atmosphere).[33] The results showed that extremely low temperature or emerging MXene flakes in ethanol could decelerate the oxidation of MXenes. Another route is to isolate the moisture from the $Ti_3C_2T_x$ MXene.[34–36] For example, sodium L-ascorbate was introduced into $Ti_3C_2T_x$ solution to protect the edges of the flakes, restricting water molecules from otherwise reactive sites.[35] Moreover, a continuous zeolitic imidazolate framework-8 layer was coated on the surface of $Ti_3C_2T_x$ MXene to prevent the permeation of water molecules.[36] However, for most cases, MXene-based materials have to work in the ambient atmosphere, which makes the aforementioned methods less effective. In this circumstance, a more efficient antioxidation strategy for MXenes has to be developed.[37,38]

[1]State Key Laboratory of Solidification Processing, Center of Advanced Lubrication and Seal Materials, School of Materials Science and Engineering, Northwestern Polytechnical University, 710072 Xi'an, China

[2]Science and Technology on Thermostructural Composite Materials Laboratory, Northwestern Polytechnical University, 710072 Xi'an, China
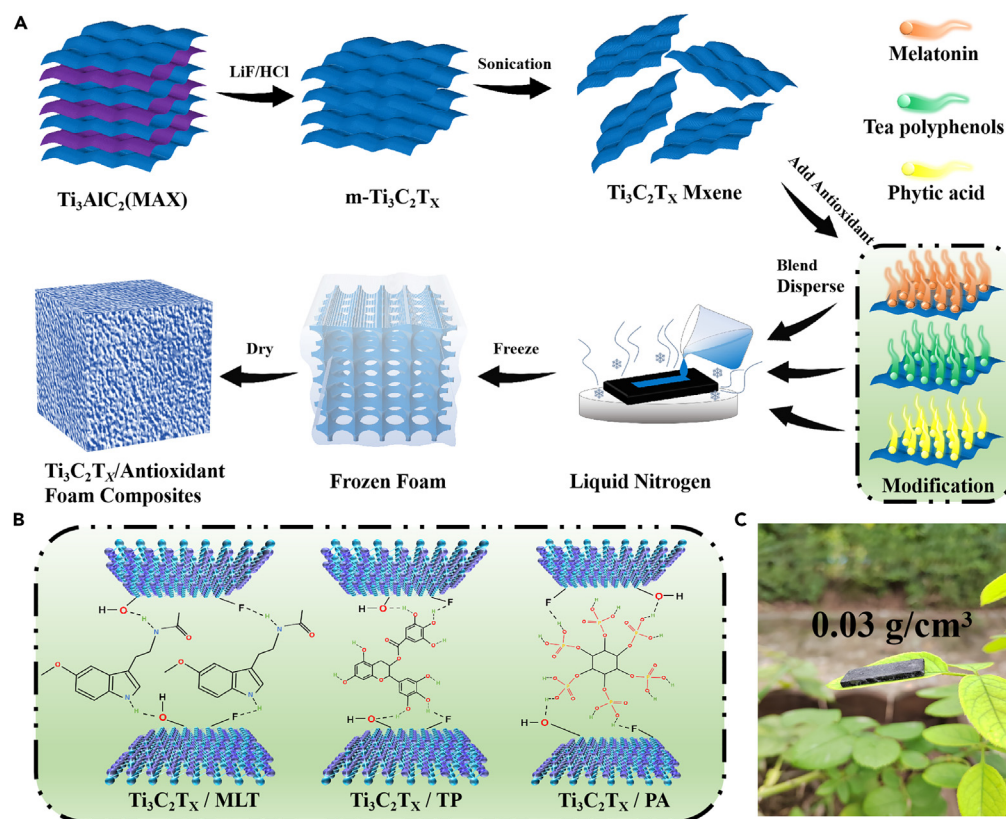
[3]Institute of Materials Science, Technische Universität Darmstadt, Alarich-Weiss-Str. 2, 64287 Darmstadt, Germany

[4]Lead contact

*Correspondence:
jianxiliu@nwpu.edu.cn (J.L.),
liuxingmin19890101@126.com (X.L.)

https://doi.org/10.1016/j.isci.2023.107176

Figure 1. Preparation process and physical view
(A) Schematic diagram of the preparation process and mechanism of the $Ti_3C_2T_x$/antioxidant foam composites.
(B) Schematic diagram of $Ti_3C_2T_x$ is linked to the antioxidants via surface hydrogen bonding.
(C) Photo image of the lightweight $Ti_3C_2T_x$/antioxidant foam composites.

Melatonin (MLT), tea polyphenols (TP), and phytic acid (PA) as natural antioxidants can effectively slow down the senility of organisms by preventing them from oxidation.[39–43] Inspired by this fact, natural antioxidants are also expected to be promising antioxidants of MXenes. Moreover, their high solubility in water facilitates the processing of composites with the MXenes. In this research, MLT, TP, and PA were employed as antioxidants to prevent the oxidation of $Ti_3C_2T_x$ MXene. $Ti_3C_2T_x$/antioxidant foam composites were prepared through the freeze-drying method. The variation in EMI SE of the as-prepared $Ti_3C_2T_x$/antioxidant foam composites as a function of exposure time in air was investigated.

RESULTS AND DISCUSSION

The morphology and composition of $Ti_3C_2T_x$/antioxidant foam composites

Figure 1A illustrates the fabrication process of the $Ti_3C_2T_x$/antioxidant foam composites. The abundant surface groups (-F, -O, and -OH) of MXene facilitated the homogeneous dispersion of $Ti_3C_2T_x$ in deionized water and the formation of hydrogen bonds with the antioxidants (Figure 1B), which could lead to a robust structure of the resultant composites.[44] Figure 1C shows a photo image of the lightweight $Ti_3C_2T_x$/antioxidant foam composites, which possesses a low density of 0.03 g/cm^3.

The cross-sectional morphology of the MXene and MXene/antioxidant foam composites before and after exposing to air was investigated with SEM (Figure 2). The SEM images in Figures 2 and S1 show that both $Ti_3C_2T_x$ and $Ti_3C_2T_x$/antioxidant foam composites exhibited similar porous structures. Figure 2A shows that the $Ti_3C_2T_x$ foam has a large-scale random structure with apertures of tens of microns in specific small regions. With the addition of antioxidants, the channels between the cellular walls became smaller, and the cellular structures in the section became intact and compact, which may be resulted from the increased hydrogen bonds that affect the packing of MXene sheets (Figure 2B). According to the high-magnification
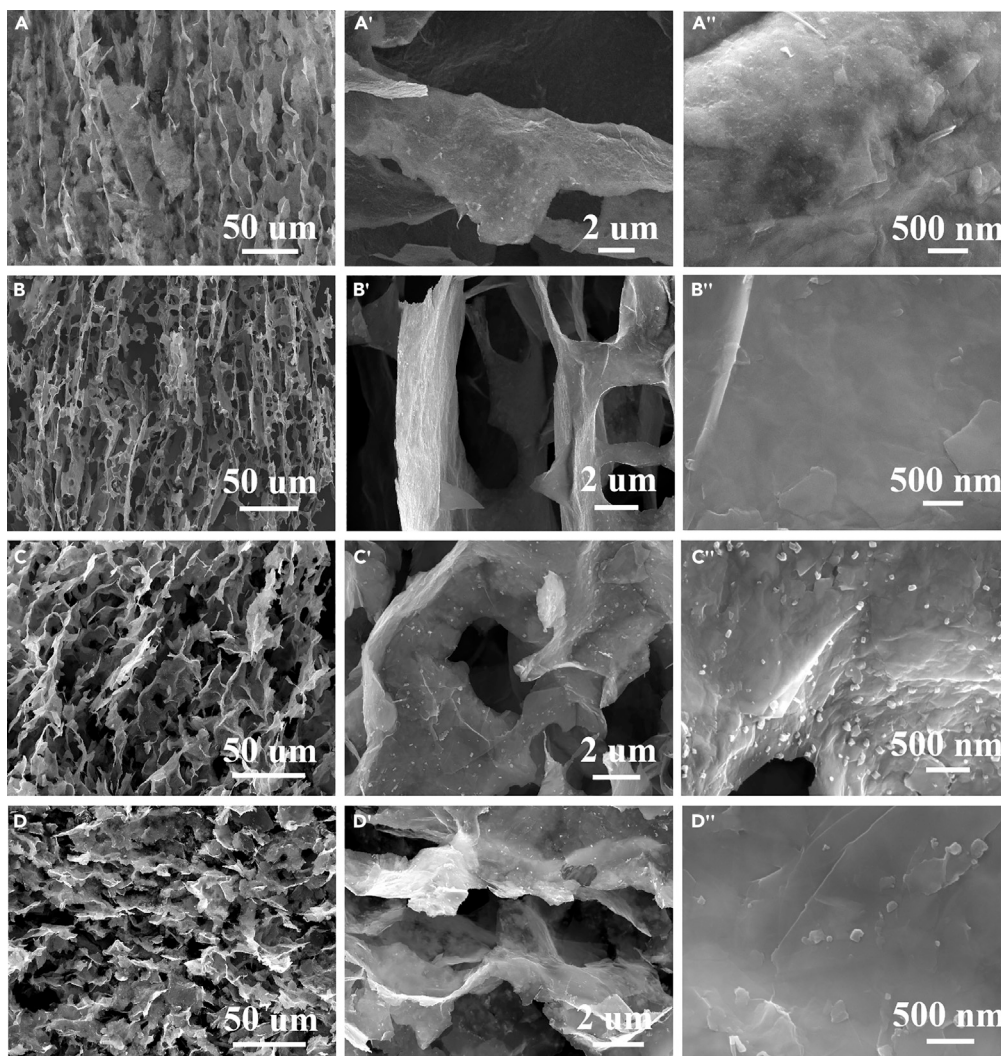
Figure 2. Cross-section SEM image of as-prepared MXene foam

(A–D) (A) Low and (A'), (A'') high-magnification SEM images of fresh $Ti_3C_2T_x$ foam, (B) Low and (B'), (B'') high-magnification SEM images of fresh $Ti_3C_2T_x$/TP foam composites, (C) Low and (C'), (C'') high-magnification SEM images of $Ti_3C_2T_x$ foam after exposing in the air for 50 days, (D) Low and (D'), (D'') high-magnification SEM images of $Ti_3C_2T_x$/TP foam composites after exposing in the air for 50 days.

SEM images, the surface structures of the $Ti_3C_2T_x$ foam and $Ti_3C_2T_x$/TP foam composites are different. A smoother surface was obtained on the surface of $Ti_3C_2T_x$/TP foam composites due to the uniform and dense coating of TP (Figure 2B''). The oxidation of $Ti_3C_2T_x$ foam in the oxygen-existing environment starts from the edge. The nucleation of TiO_2 uniformly dispersed on the $Ti_3C_2T_x$ sheets (Figure 2C). However, $Ti_3C_2T_x$/TP foam composites have a decreased oxidation behavior. Almost no TiO_2 can be found on the surface of $Ti_3C_2T_x$/TP foam composites (Figure 2D). The microstructures of $Ti_3C_2T_x$/MLT and $Ti_3C_2T_x$/PA foam composites after oxidation in Figure S1 show similar results.

The phase and chemical composition evolution of the $Ti_3C_2T_x$ and $Ti_3C_2T_x$/antioxidant foam composites as a function of exposing time in air were investigated. Figure 3 shows the X-ray diffraction (XRD) and X-ray photoelectron spectroscopy (XPS) spectra of the $Ti_3C_2T_x$ foam and $Ti_3C_2T_x$/antioxidant foam composites after exposing in air for 0, 20, and 50 days. Based on Bragg's law (Figure 3A), the interspace of the few-layered $Ti_3C_2T_x$ MXene is approximately 1.22 nm through the calculation of the (002) peak at 7.23°.[45] After 50 days, the intensity of characteristic peak from Ti_3C_2 decreased significantly, indicating a fast degradation of the $Ti_3C_2T_x$. For the $Ti_3C_2T_x$/TP foam composites, the (002) peak shifted to the low angle range
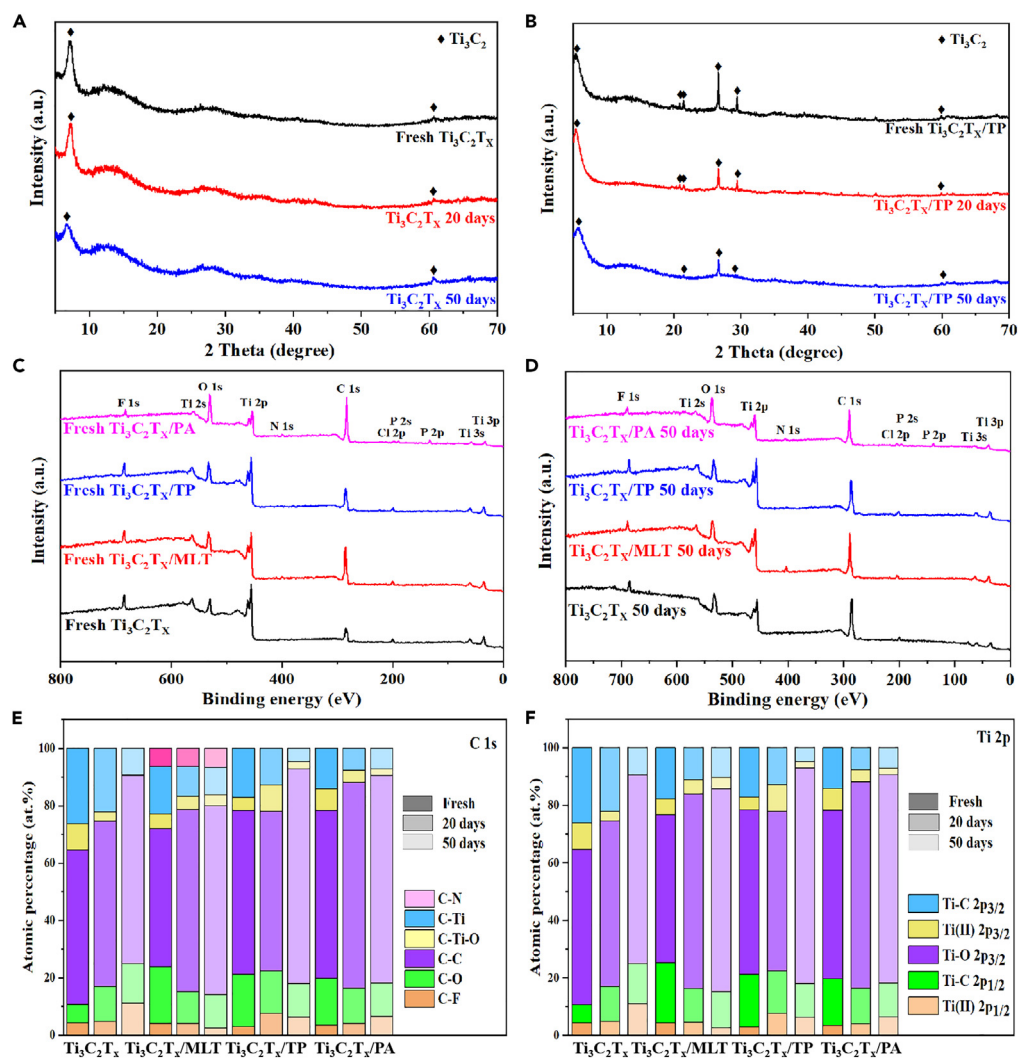
Figure 3. Chemical composition of Ti$_3$C$_2$T$_x$ foam and Ti$_3$C$_2$T$_x$/antioxidant foam composites after being stored for different times

(A–F) XRD patterns of (A) Ti$_3$C$_2$T$_x$ and (B) Ti$_3$C$_2$T$_x$/TP foam composites. Full spectrum of XPS in (C) fresh and (D) aged for 50 days. XPS peak fitting results in the (E) C 1s and (F) Ti 2p regions. Histogram showing atomic percentages of C-Ti, C-Ti-O, C-C, C-N, C-O, and C-N obtained from the C 1s region and the atomic percentages of Ti-O 2p$_{3/2}$, Ti(II) 2p$_{1/2}$, Ti(II) 2p$_{3/2}$, Ti-C 2p$_{1/2}$, and Ti-C 2p$_{3/2}$ obtained from deconvoluted Ti 2p.

(Figure 3B), which predicates that the interspace of the Ti$_3$C$_2$T$_x$ sheets decreased.[46–49] In addition, the (008) peak at 26.63° appeared, which is resulted from change in the crystal orientation of Ti$_3$C$_2$T$_x$. After exposing in air for 50 days, the characteristic peak of Ti$_3$C$_2$T$_x$ in Ti$_3$C$_2$T$_x$/TP foam composites is still very strong, demonstrating a decreased decomposition degree. Meanwhile, the (002) peak shifted to a higher degree due to the consumption of TP during the oxidation process. Figure S2 shows that MLT and PA can also effectively slow down the oxidation process of Ti$_3$C$_2$T$_x$. In Figure S3, the Ti$_3$C$_2$T$_x$ and Ti$_3$C$_2$T$_x$/antioxidant foam composites exhibited similar Raman spectra, where both characteristic peaks from Ti$_3$C$_2$T$_x$ and graphitic carbon were detected. After exposing in air for 50 days, the intensity of the corresponding peaks from Ti$_3$C$_2$T$_x$ decreased significantly while signals from graphitic carbon increased accordingly. The ratio of I$_D$/I$_G$ increased from 0.929 to 0.967. Notably, the I$_D$/I$_G$ value of Ti$_3$C$_2$T$_x$/antioxidant foam composites did not increase since the oxidation process of Ti$_3$C$_2$T$_x$ was inhibited.

To investigate the evolution of the chemical bonds and compositions in the Ti$_3$C$_2$T$_x$/TP foam composites, XPS with binding energies ranging from 0 to 800 eV was employed (Figure 3C). Peaks for Ti, C, O, and F

were observed in all materials. A new peak at ~400 eV corresponding to N 1s appeared in $Ti_3C_2T_x$/MLT and $Ti_3C_2T_x$/PA, which can be contributed to MLT and PA molecules, respectively (the peak belonging to P appeared in $Ti_3C_2T_x$/PA). To investigate the oxidation state of the MXene sheets, the XPS spectra of $Ti_3C_2T_x$ and $Ti_3C_2T_x$/antioxidant foam composites after exposing in air for 50 days are plotted in Figure 3D. The peak at ~284.8 eV related to C 1s is greatly enhanced while the peak intensity of Ti 2s is obviously weakened, which can be attributed to the severe oxidation of $Ti_3C_2T_x$.[50–52] For the $Ti_3C_2T_x$/antioxidant foam composites, the intensity of corresponding peaks did not change obviously, which indicates that the 2D structure of the $Ti_3C_2T_x$ sheet did not exhibit obvious change,[53] and the oxidation degree was weakened, well consistent with the XRD and SEM results. To further analyze the chemical compositions and atomic fractions of $Ti_3C_2T_x$, $Ti_3C_2T_x$/MLT, $Ti_3C_2T_x$/TP, and $Ti_3C_2T_x$/PA exposed in air for different time, peak fitting was performed on the C 1s and Ti 2p spectra. For all foams (fresh and 20 and 50 days), five bonds were deconvoluted from the C 1s region (Figures S4A–S4D), including C-F (288.8 eV), C-O (286.1 eV), C-C (284.8 eV), C-Ti-O (283.5 eV), and C-Ti (281.6 eV).[54,55] After 50 days in air, $Ti_3C_2T_x$, $Ti_3C_2T_x$/MLT, $Ti_3C_2T_x$/TP, and $Ti_3C_2T_x$/PA showed different degrees of oxidation, and the peak value of C-Ti decreased generally, and C-C increased sharply, which should be attributed to the reduction of $Ti_3C_2T_x$ and the formation of amorphous carbon. In particular, C-N (285.4 eV) appeared in the peak fitting of $Ti_3C_2T_x$/MLT because the MLT molecules contained a large number of C-N bonds (Figure S4B), and the addition of TP introduced a large amount of C-O (Figure S4C). Five bonds were deconvoluted from the Ti 2p region (Figures S4E–S4H), including Ti(II) $2p_{1/2}$ (462.0 eV), Ti-C $2p_{1/2}$ (461.2 eV), Ti-O (458.4 eV), Ti(II) $2p_{3/2}$ (455.5 eV), and Ti-C $2p_{3/2}$ (454.8 eV).[56] The sharp increase in Ti-O bond is mainly attributed to the formation of TiO_2. Figures 3E and 3F unambiguously demonstrate the change in atomic percentage of various components with the prolongation of oxidation time. The C-Ti bond in $Ti_3C_2T_x$ decreased significantly after exposing in air (from 26.21% to 9.28%) while the C-Ti-O bond decreased greatly from 9.16% to 0.14%, and the C-C bond increased (from 53.84% to 65.52%), and the Ti-O in the +4 state increased sharply from 5.44% to 10.70%. The C-N in $Ti_3C_2T_x$/MLT remained at approximately 6.5%, the C-Ti did not decrease (from 13.46% to 13.88%), and the C-Ti-O bond decreased, but not all degraded (significantly decreased from 9.79% to 5.69%). The C-C also increased significantly (from 64.01% to 65.95%), and Ti-O in the +4 state increased slightly from 5.44% to 10.70%. The addition of TP and PA showed the same change rule with MLT, indicating that the introduction of antioxidants inhibited the oxidation of $Ti_3C_2T_x$. It can be seen from the SEM that regardless of the severe oxidation of $Ti_3C_2T_x$, the skeleton structure of the foam is always well reserved (Figure 2C).

The nanostructure evolution of the $Ti_3C_2T_x$ and $Ti_3C_2T_x$/PA foam composites was investigated with transmission electron microscopy (TEM). In the low-resolution TEM image (Figure S5), MXene layers with a diameter of 3 μm can be seen. In the high-resolution TEM image (Figure 4A), a uniform crystalline phase of $Ti_3C_2T_x$ was observed, consistent with the TEM image of $Ti_3C_2T_x$ MXene on previous.[57] For TEM image of fresh $Ti_3C_2T_x$/TP foam composites, no difference from the pristine $Ti_3C_2T_x$ was found. After exposing in air for 50 days, obvious phase evolution resulted from the decomposition of the $Ti_3C_2T_x$ was observed on the edge area. Disordered carbon and TiO_2 nanoparticles were observed in between the Ti_3C_2 phase.[58,59] The formation of carbon and TiO_2 phases was resulted from the oxidation reaction of $Ti_3C_2T_x$ with O_2 and H_2O molecules.[39] However, for the $Ti_3C_2T_x$/TP foam composites, though the edge of $Ti_3C_2T_x$/TP was also oxidized, the oxidation reaction did not proceed to the deep area of $Ti_3C_2T_x$ due to the protection of TP molecules. Figure 4E shows the EDS spectrum of the $Ti_3C_2T_x$/PA foam composites after exposing in air for 50 days. As a characteristic element in PA, phosphate element is uniformly dispersed on the $Ti_3C_2T_x$ sheet, and the element diagrams of Ti and O prove that the oxidation still started from the edge. As expected, at the edge of the $Ti_3C_2T_x$ sheet, TiO_2 and disordered carbon were formed. It has been reported that phosphate ions can coat the edges of individual $Ti_3C_2T_x$,[39] preventing the entering of O_2 and water molecules, therefore slow down their oxidation even if placed in air or moisture atmosphere for several weeks. As far as $Ti_3C_2T_x$/MLT is concerned, the strong reducibility of MLT is used to protect $Ti_3C_2T_x$. After 50 days in air, TiO_2 crystal phase was hardly found in the TEM image of the $Ti_3C_2T_x$/MLT foam composites, and only a small amount of free carbon appeared, which can be understood that carbon phase generated during the decomposition of MLT itself (as shown in Figure S6).

Mechanical properties

The mechanical property of the prepared foam composites is an important factor for the evaluation of the materials. The compressive resilience and mechanical strength of each batch of foam composites (Figure S7) was characterized with a computerized universal material testing machine (HZ-10048, 50 N).
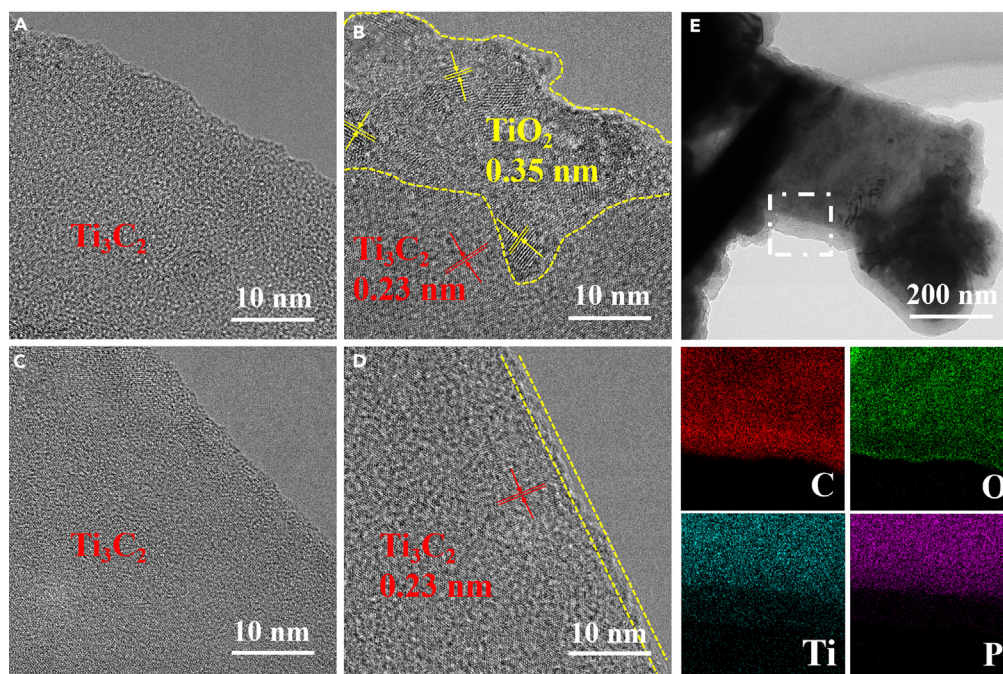
Figure 4. Nanostructure evolution of the Ti$_3$C$_2$T$_x$ and Ti$_3$C$_2$T$_x$/PA foam composites
TEM image of Ti$_3$C$_2$T$_x$ foam (A) fresh, (B) 50 days, Ti$_3$C$_2$T$_x$/TP (C) fresh, (D) 50 days, (E) EDS spectra of Ti$_3$C$_2$T$_x$/PA after 50 days of aging.

Each sample was measured at a thickness of 2 mm, via the "load-unload" method. Deformation ratios of 25%, 50%, and 75% were used respectively to detect the compression rebound rate of the foams. As shown in Figure 5A, after the Ti$_3$C$_2$T$_x$-based composites were pressed to deform by 25%, the foam materials returned to the initial position and loads again. When the deformation ratio was 16%, stress was detected. The rebound rate under 25% deformation was 9%. Similarly, when the deformation rates were 50% and 75%, the rebounding rates were 12% and 15%, respectively, which followed a proportional relationship. With the addition of antioxidants, the corresponding foam materials still possessed good compression rebounding rate (Figures 5B–5D). The strain-stress curves are shown in Figure 5. The compressive strength of the fresh Ti$_3$C$_2$T$_x$ foam was 4.0×10^{-2} MPa, while the compressive strength of the Ti$_3$C$_2$T$_x$/MLT, Ti$_3$C$_2$T$_x$/TP, and Ti$_3$C$_2$T$_x$/PA treatments increased to 6.0×10^{-2}, 1.4×10^{-1}, and 1.0×10^{-1} MPa, respectively. Figure S8 shows that after aging 50 days in air, the compression resilience performance did not change obviously. The enhancement of mechanical properties can be contributed to the interaction between Ti$_3$C$_2$T$_x$ sheets and antioxidant.[55]

Electromagnetic interference shielding mechanisms and effectiveness

Figure 6 shows the SE$_T$, SE$_R$, and SE$_A$ of all batches of 20%-Ti$_3$C$_2$T$_x$/antioxidant foam composites as a function of exposure time (0, 20, and 50 days) in air. As shown in Figure 6A, the SE$_T$ of fresh Ti$_3$C$_2$T$_x$ foam (control test sample) can reach as high as 49.15 dB at a material thickness of 2.0 mm. Meanwhile, the SE$_T$ of Ti$_3$C$_2$T$_x$ foam composites with 20% mass fraction of MLT, TP, and PA was 49.94, 49.54, and 49.72 dB, respectively. After exposing in air for 20 days, the SE$_T$ of the pure Ti$_3$C$_2$T$_x$ foam decreased significantly from 49.15 to 40.08 dB due to the fast degradation of Ti$_3$C$_2$T$_x$ in the air, which was confirmed by XRD (Figure 3A), Raman (Figure S3A), XPS (Figure 3D), and TEM (Figure 4B). However, for the 20%-Ti$_3$C$_2$T$_x$/MLT and 20%-Ti$_3$C$_2$T$_x$/TP foam composites, the fading rate of SE$_T$ was significantly slowed down. For example, the SE$_T$ of 20%-Ti$_3$C$_2$T$_x$/MLT and 20%-Ti$_3$C$_2$T$_x$/TP slightly decreased from 49.94 to 49.54–44.94 dB and 44.02 dB due to the protection of antioxidants. However, the SE$_T$ of 20%-Ti$_3$C$_2$T$_x$/PA decreased from 49.72 to 39.12 dB, which was even fast than the pure MXene foam. The SE$_T$ of 20%-Ti$_3$C$_2$T$_x$/PA was 43.99 dB at 10 days. With further exposing time in air, the consumption of PA led to the exposure of Ti$_3$C$_2$T$_x$ to air, and the decreasing of SE$_T$ was consistent with that of pure Ti$_3$C$_2$T$_x$. The SE$_T$ of each batch of samples continued to decrease after 50 days of aging (Figure 6C). However, the EMI SE decreasing rate of 20%-Ti$_3$C$_2$T$_x$/MLT and 20%-Ti$_3$C$_2$T$_x$/TP foam composites was always slower than that of pure Ti$_3$C$_2$T$_x$
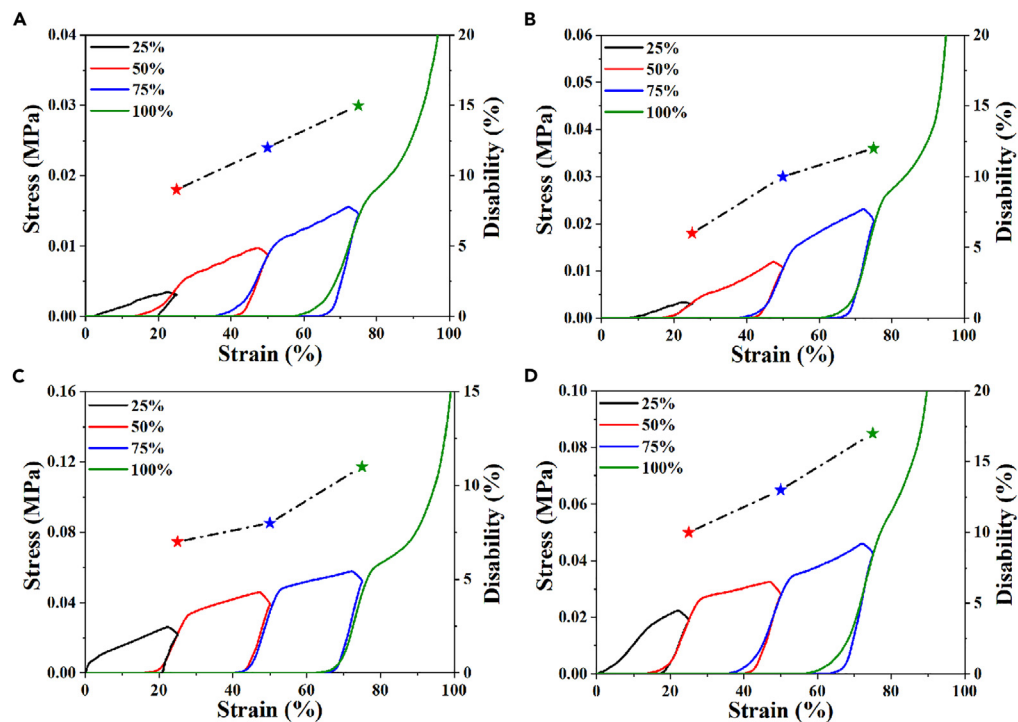
Figure 5. Mechanical properties of Ti₃C₂Tₓ foam and Ti₃C₂Tₓ/antioxidant foam composites
Stress-strain curves of each batch of fresh foam composites: (A) Ti₃C₂Tₓ, (B) Ti₃C₂Tₓ/MLT, (C) Ti₃C₂Tₓ/TP, and (D) Ti₃C₂Tₓ/PA. The symbol of stars represents the rebound rate under different compressions. 25% (red), 50% (blue), and 75% (green).

foam. This phenomenon can be explained by the reduced degree of MXene degradation observed in the XRD, XPS, and TEM results.

Figures 6D–6F present the SE_R of all batches of 20%-Ti₃C₂Tₓ/antioxidant foam composites as a function of exposing time in air. Among all samples, the pure Ti₃C₂Tₓ foam exhibited the highest SE_R value of 11.82 dB due to the high conductivity of MXene (Figure 6D). With the improvement of the impedance matching by incorporation of the polymeric antioxidant, the SE_R of the Ti₃C₂Tₓ/antioxidant foam composites decreased obviously. For example, the SE_R of 20%-Ti₃C₂Tₓ/PA was 9.95 dB. Due to the oxidation of the Ti₃C₂Tₓ in the foams, the SE_R of all composites showed a decreasing trend. As expected, the SE_R of the pure MXene foam showed the largest electromagnetic (EM) performance fading rate and the SE_R decreased to 8.50 dB. The SE_A and SE_T of all batches of 20%-Ti₃C₂Tₓ/antioxidant foam composites shared the same varying tendency. The addition of antioxidants makes the Ti₃C₂Tₓ foam composites have an increased SE_A. We found 20%-Ti₃C₂Tₓ/TP exhibited the largest SE_A, which was approximately 42.28 dB. This phenomenon can be explained by the SEM results that the 20%-Ti₃C₂Tₓ/TP foam composites possess a more compact structure. With the prolonged exposing time, the SE_A decreasing rate of 20%-Ti₃C₂Tₓ/MLT and 20%-Ti₃C₂Tₓ/TP foam composites is always slower than that of pure Ti₃C₂Tₓ foam. The 20%-Ti₃C₂Tₓ/PA foam composites due to the oxidation of PA, and the SE_A are eventually lower than that of pure Ti₃C₂Tₓ foam.

Figure 7 shows the mean EMI SE values of all batches of Ti₃C₂Tₓ/TP foam composites as a function of exposing time in air. For the fresh Ti₃C₂Tₓ/TP foam composites, the mean value of EMI SE decreased with increasing TP content in the foams (Figure 7A). After exposure to air for 50 days, the average EMI SE of control test Ti₃C₂Tₓ foam decreased significantly from 49.15 to 36.11 dB due to the severe oxidation of Ti₃C₂Tₓ in air, resulting in an EMI SE loss of 26.53%. For the Ti₃C₂Tₓ/TP foam composites, the EMI SE showed a rather slow fading rate within the 50 days due to the protection of TP. However, with the increasing TP content in the foam, the EMI loss rate increases. It has been reported that the reaction with H_2O in air also leads to the degradation of MXenes,[57] besides the oxidation of O_2. Based on this understanding, we propose this is resulted from the reaction of Ti₃C₂Tₓ with the H_2O molecule absorbed by
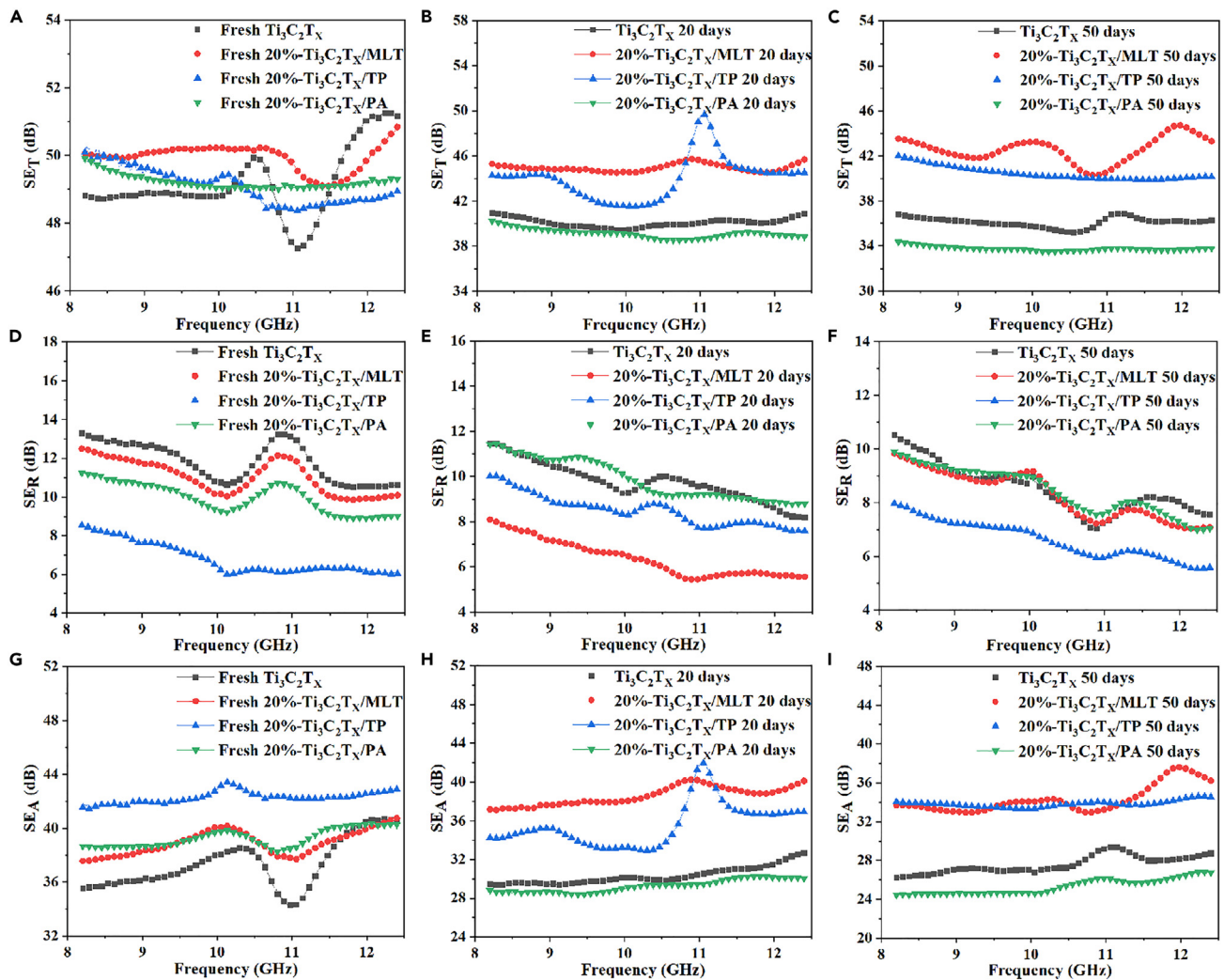
Figure 6. The EMI shielding performance of the $Ti_3C_2T_x$/antioxidant foam composites in the X-band
Pure $Ti_3C_2T_x$ and foam composites with 20% antioxidant addition exposed to air (A) fresh, (B) 20 days, (C) 50 days; SE_R of samples (D) fresh, (E) 20 days, (F) 50 days; and SE_A of samples (G) fresh, (H) 20 days, (I) 50 days.

hydrophilic TP. For the fresh $Ti_3C_2T_x$/MLT foam composites, the average value of EMI SE decreased with increasing MLT content in the resulting foam (Figure S9), and the overall varying tendency is consistent with that of $Ti_3C_2T_x$/TP foam composites. Different from the other two foam composites, $Ti_3C_2T_x$/PA showed an inferior EMI SE and larger EMI SE loss rate. Among them, the fresh $Ti_3C_2T_x$/PA showed the best EMI SE performance. With increasing PA content, the SE_T loss rate increased gradually (Figure S10). The main reason can be attributed to the addition of PA in the form which delayed the oxidation process. A large number of water molecules were absorbed at the beginning, and the PA adsorbed between the $Ti_3C_2T_x$ sheet was oxidized in a relatively short time and lost its protective effect on $Ti_3C_2T_x$.

Figure 8A is a schematic diagram of the electromagnetic shielding mechanism of $Ti_3C_2T_x$/antioxidant foam composites. Due to the high electrical conductivity of $Ti_3C_2T_x$/antioxidant foam composites, the incident EM waves are reflected immediately.[60,61] Also, the EM waves that enter the interior of the material can be further absorbed through the dipole loss and carrier loss caused by positive- and negative-charged electrons on the $Ti_3C_2T_x$ surface. It is clear that in $Ti_3C_2T_x$/antioxidant foam composites the porous structure created by the doping of antioxidants plays a decisive role in the attenuation of electromagnetic waves through enhanced absorption. The resulting interfacial polarization, scattering effects, and electron band mixing have a significant impact on the dielectric properties, while the EMI shielding performance of the
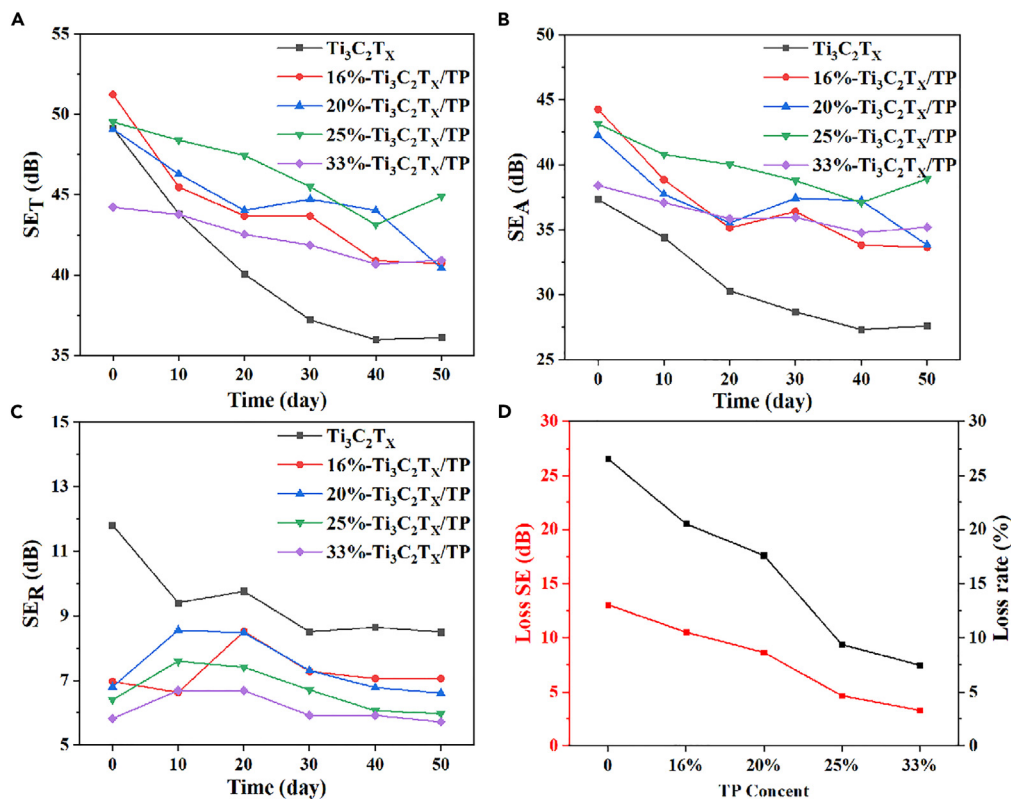
Figure 7. Durability of the antioxidant modified MXenes for EMI SE
(A–D) (A) SE_T, (B) SE_A, (C) SE_R, and (D) EMI SE fade rate and fade value of all batches of $Ti_3C_2T_x$/TP foam composites as a function of air exposure time.

composite foam is greatly improved by the presence of a large number of interfaces in the pores, which extend the transmission and attenuation routes through multiple scattering and reflection. In addition, composite foams can be assembled into porous layered structures that further contribute to the interfacial scattering effect.[62–64] For the different antioxidant content of the composite foams, the highest EMI SE is achieved at 20%, 25%, and 16% for MLT, TP, and PA, respectively. Table S1 compares the EMI SE of this work with other electromagnetic shielding materials.[31,65–69]

The degradation behavior of $Ti_3C_2T_x$ MXene solutions is such that when dissolved oxygen and water are present, the former preferably reacts with the most active flake edges, leading to the formation of anatase (TiO_2). The process is shown in Figure 8B, where for $Ti_3C_2T_x$ foams, water and oxygen molecules begin to oxidize the MXene at the edges and rapidly diffuse to the interior. The reaction led by water could be written as[57]

$$Ti_3C_2O_2 + 4H_2O = 3TiO_2 + 2C + 4H_2$$
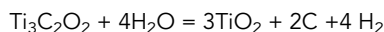
In order to avoid degradation altogether, we avoid oxidation by adding antioxidants. Through its XRD and SEM, we found that $Ti_3C_2T_x$ can still maintain good morphology after a period of oxidation (Figures 2 and 3). The addition of antioxidants effectively seals the edges of the $Ti_3C_2T_x$ sheet and the added antioxidants can improve the stability of $Ti_3C_2T_x$ MXene in use by their own consumption and protect $Ti_3C_2T_x$ MXene from oxidation.

Conclusion

We developed a new strategy to achieve the long-term stability of MXene composite foam based on $Ti_3C_2T_x$ modified with melatonin, tea polyphenols, and phytic acid. The composite was analyzed to significantly reduce the EMI SE fading rates and improve the EMI SE stability. After 50 days of air exposure, the EMI SE of $Ti_3C_2T_x$ foam decreased from 49.15 to 36.11 dB. When the $Ti_3C_2T_x$ was modified by MLT with
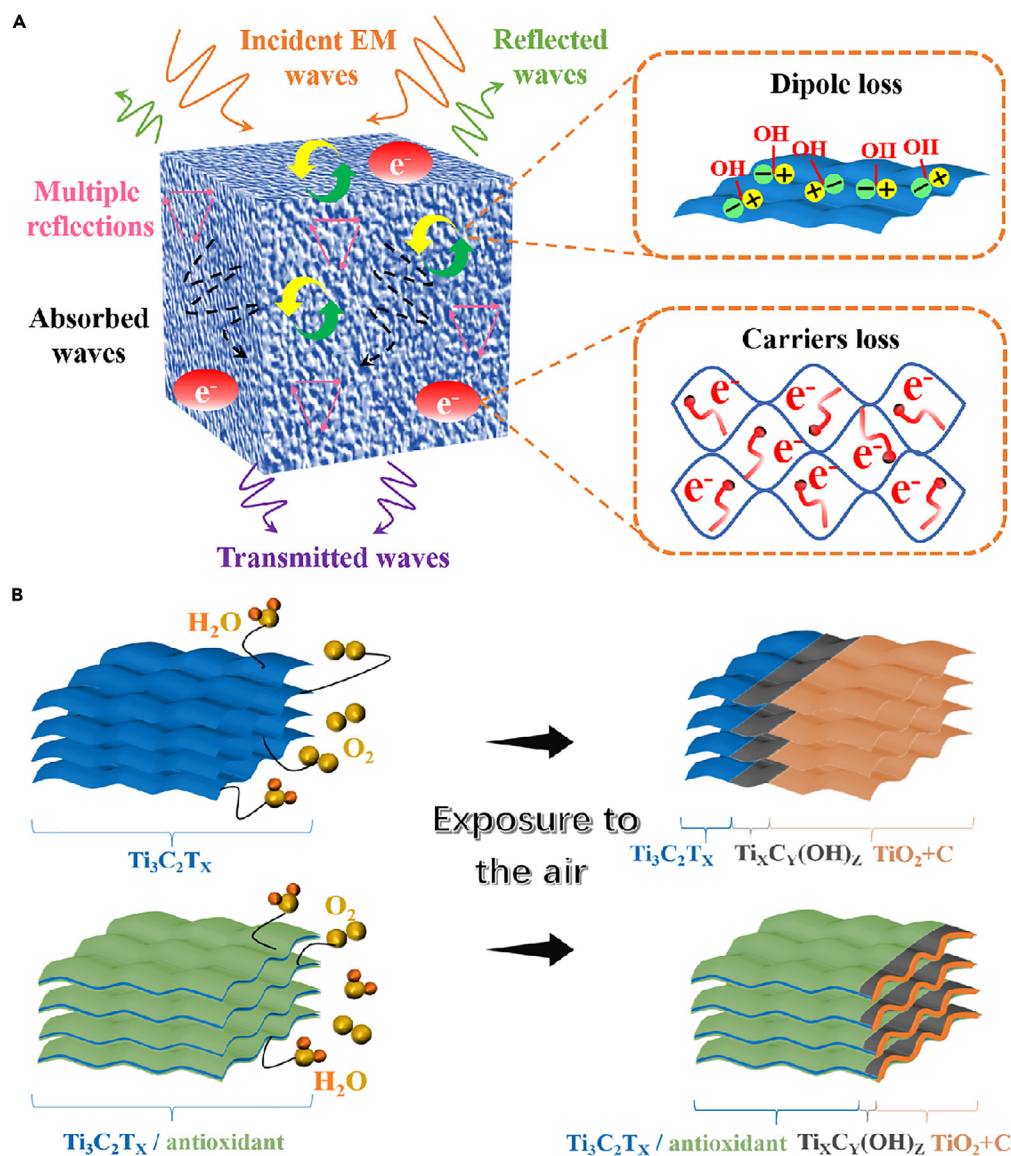
Figure 8. Schematic illustration of EMI shielding mechanism for the Ti₃C₂Tₓ/antioxidant foam composites

(A) electromagnetic shielding mechanism and (B) anti-oxidant protection mechanism.

content of 20%, the EMI SE was greatly enhanced to be 42.56 dB after 50 days. For $Ti_3C_2T_x$ containing 25 wt % of TP, the EMI SE amounts 44.90 dB after 50 days. For $Ti_3C_2T_x$ with a content of 16 wt % PA, the EMI SE remained as high as 49.09 dB after 10 days. Due to the addition of the molecular natural antioxidants, the $Ti_3C_2T_x$ sheet and edges were sealed by the molecules, which protected the $Ti_3C_2T_x$ from oxidation by oxygen and from hydrolysis by water. In addition, the compressive strength of the fresh $Ti_3C_2T_x$ foam was 4.0×10^{-2} MPa, while the compressive strength of the $Ti_3C_2T_x$/MLT, $Ti_3C_2T_x$/TP, and $Ti_3C_2T_x$/PA foam composites increased to 6.0×10^{-2}, 1.4×10^{-1}, and 1.0×10^{-1} MPa, respectively, indicating improved mechanical stability of the foams. This work contributes i) to broaden the fundamental knowledge of MXenes and ii) to further develop the potential application of MXene-based $Ti_3C_2T_x$ foams in harsh environments.

STAR★METHODS

Detailed methods are provided in the online version of this paper and include the following:

- KEY RESOURCES TABLE

- RESOURCE AVAILABILITY
  - Lead contact
  - Materials availability
  - Data and code availability
- METHOD DETAILS
  - Materials
  - Synthesis of few-layered $Ti_3C_2T_x$ MXene flakes
  - Preparation of $Ti_3C_2T_x$/antioxidant and $Ti_3C_2T_x$ foam composites
  - Materials characterization
  - Measurement of EMI shielding performance

AUTHOR CONTRIBUTIONS

G.W.: Data curation, Investigation, Validation, Writing-original draft. M.L.: Data curation, Investigation. J.L.: Conceptualization, Methodology. F.Y.: Conceptualization, Methodology. L.C.: Conceptualization, Investigation. X.F.: Investigation, Methodology. X.L.: Conceptualization, Methodology, Validation, Investigation, Writing-original draft, Writing-review & editing, Funding acquisition. R.R.: Investigation, Methodology.

DECLARATION OF INTERESTS

The authors declare that they have no known competing financial interests or personal relationships that could have appeared to influence the work reported in this paper.

REFERENCES

1. Liang, H., Chen, G., Liu, D., Li, Z., Hui, S., Yun, J., Zhang, L., and Wu, H. (2022). Exploring the Ni 3d Orbital Unpaired Electrons Induced Polarization Loss Based on Ni Single-Atoms Model Absorber. Adv. Funct. Mater. *33*, 2212604.

2. Liang, H., Zhang, L., and Wu, H. (2022). Exploration of Twin-Modified Grain Boundary Engineering in Metallic Copper Predominated Electromagnetic Wave Absorber. Small *18*, 2203620.

3. Li, C., Qi, X., Gong, X., Peng, Q., Chen, Y., Xie, R., and Zhong, W. (2022). Magnetic-dielectric synergy and interfacial engineering to design yolk-shell structured CoNi@void@C and CoNi@void@C@MoS2 nanocomposites with tunable and strong wideband microwave absorption. Nano Res. *15*, 6761–6771.

4. Xiao, J., Qi, X., Gong, X., Peng, Q., Chen, Y., Xie, R., and Zhong, W. (2022). Defect and interface engineering in core@shell structure hollow carbon@MoS2 nanocomposites for boosted microwave absorption performance. Nano Res. *15*, 7778–7787.

5. Li, M., Chai, N., Liu, X., Xie, W., Wang, G., Qu, F., Chen, Y., Fan, X., Weidenkaff, A., and Riedel, R. (2021). Sustainable paper templated ultrathin, light-weight and flexible niobium carbide based films against electromagnetic interference. Carbon *183*, 929–939.

6. Li, M., Fan, X., Xu, H., Ye, F., Xue, J., Li, X., and Cheng, L. (2020). Controllable synthesis of mesoporous carbon hollow microsphere twined by CNT for enhanced microwave absorption performance. Neurosci. Biobehav. Rev. *116*, 164–181.

7. Liu, J., Zhang, H.B., Sun, R., Liu, Y., Liu, Z., Zhou, A., and Yu, Z.Z. (2017). Hydrophobic, Flexible, and Lightweight MXene Foams for High-Performance Electromagnetic-Interference Shielding. Adv. Mater. *29*, 1702367.

8. Li, X., Li, M., Lu, X., Zhu, W., Xu, H., Xue, J., Ye, F., Liu, Y., Fan, X., and Cheng, L. (2021). A sheath-core shaped ZrO2-SiC/SiO2 fiber felt with continuously distributed SiC for broadband electromagnetic absorption. Chem. Eng. J. *419*, 129414.

9. Lu, X., Li, X., Wang, Y., Hu, W., Zhu, W., Zhu, D., and Qing, Y. (2022). Construction of ZnIn2S4 nanosheets/3D carbon heterostructure with Schottky contact for enhancing electromagnetic wave absorption performance. Chem. Eng. J. *431*, 134078.

10. Yang, P.A., Ruan, H., Sun, Y., Li, R., Lu, Y., and Xiang, C. (2020). Excellent microwave absorption performances of high length-diameter ratio iron nanowires with low filling ratio. Nanotechnology *31*, 395708.

11. Kong, L., Luo, S., Zhang, S., Zhang, G., and Liang, Y. (2023). Ultralight pyrolytic carbon foam reinforced with amorphous carbon nanotubes for broadband electromagnetic absorption. Int. J. Miner. 30, 570–580.

12. Wu, M., Darboe, A.K., Qi, X., Xie, R., Qin, S., Deng, C., Wu, G., and Zhong, W. (2020). Optimization, selective and efficient production of CNTs/Co$_x$Fe$_{3-x}$O$_4$ core/shell nanocomposites as outstanding microwave absorbers. J. Mater. Chem. C 8, 11936–11949.

13. Kong, L., Zhang, S., Liu, Y., Xu, H., Fan, X., and Huang, J. (2023). Flexible CNTs/CNF-WPU aerogel for smart electromagnetic wave absorbing with tuning effective absorption bandwidth. Carbon 207, 13–22.

14. Hu, F., Zhang, F., Wang, X., Li, Y., Wang, H., Zhang, R., Li, H., and Fan, B. (2022). Ultrabroad band microwave absorption from hierarchical MoO$_3$/TiO$_2$/Mo$_2$TiC$_2$T$_x$ hybrids via annealing treatment. J. Adv. Ceram. 11, 1466–1478.

15. Song, L., Fan, B., Chen, Y., Gao, Q., Li, Z., Wang, H., Zhang, X., Guan, L., Li, H., and Zhang, R. (2022). Ultralight and hyperelastic SiC nanofiber aerogel spring for personal thermal energy regulation. J. Adv. Ceram. 11, 1235–1248.

16. Niu, H., Tu, X., Zhang, S., Li, Y., Wang, H., Shao, G., Zhang, R., Li, H., Zhao, B., and Fan, B. (2022). Engineered core-shell SiO$_2$@Ti$_3$C$_2$T$_x$ composites: Towards ultra-thin electromagnetic wave absorption materials. Chem. Eng. J. 446, 137260.

17. Ye, F., Song, Q., Zhang, Z., Li, W., Zhang, S., Yin, X., Zhou, Y., Tao, H., Liu, Y., Cheng, L., et al. (2018). Direct Growth of Edge-Rich Graphene with Tunable Dielectric Properties in Porous Si$_3$N$_4$ Ceramic for Broadband High-Performance Microwave Absorption. Adv. Funct. Mater. 28, 1707205.

18. Fan, Z., Wang, D., Yuan, Y., Wang, Y., Cheng, Z., Liu, Y., and Xie, Z. (2020). A lightweight and conductive MXene/graphene hybrid foam for superior electromagnetic interference shielding. Chem. Eng. J. 381, 122696.

19. Li, M., Zhu, W., Li, X., Xu, H., Fan, X., Wu, H., Ye, F., Xue, J., Li, X., Cheng, L., and Zhang, L. (2022). Ti$_3$C$_2$T$_x$/MoS$_2$ Self-Rolling Rod-Based Foam Boosts Interfacial Polarization for Electromagnetic Wave Absorption. Adv. Sci. 9, 2201118.

20. Yun, T., Kim, J.S., Shim, J., Choi, D.S., Lee, K.E., Koo, S.H., Kim, I., Jung, H.T., Yoo, H.W., Jung, H.J., and Kim, S.O. (2017). Ultrafast Interfacial Self-Assembly of 2D Transition Metal Dichalcogenides Monolayer Films and Their Vertical and In-Plane Heterostructures. ACS Appl. Mater. Interfaces 9, 1021–1028.

21. Hu, F., Wang, X., Bao, S., Song, L., Zhang, S., Niu, H., Fan, B., Zhang, R., and Li, H. (2022). Tailoring electromagnetic responses of delaminated Mo$_2$TiC$_2$T$_x$ MXene through the decoration of Ni particles of different morphologies. Chem. Eng. J. 440, 135855.

22. Du, H., Zhang, Q., Zhao, B., Marken, F., Gao, Q., Lu, H., Guan, L., Wang, H., Shao, G., Xu, H., et al. (2021). Novel hierarchical structure of MoS$_2$/TiO$_2$/Ti$_3$C$_2$T$_x$ composites for dramatically enhanced electromagnetic absorbing properties. J. Adv. Ceram. 10, 1042–1051.

23. Shi, Y., Xiang, Z., Cai, L., Pan, F., Dong, Y., Zhu, X., Cheng, J., Jiang, H., and Lu, W. (2022). Multi-interface assembled N-doped MXene/HCFG/AgNW films for wearable electromagnetic shielding devices with multimodal energy conversion and healthcare monitoring performances. ACS Nano 16, 7816–7833.

24. Cao, W.T., Chen, F.F., Zhu, Y.J., Zhang, Y.G., Jiang, Y.Y., Ma, M.G., and Chen, F. (2018). Binary Strengthening and Toughening of MXene/Cellulose Nanofiber Composite Paper with Nacre-Inspired Structure and Superior Electromagnetic Interference Shielding Properties. ACS Nano 12, 4583–4593.

25. Weng, G., Li, J., Alhabeb, M., Karpovich, C., Wang, H., Lipton, J., Maleski, K., Kong, J., Shaulsky, E., Elimelech, M., et al. (2018). Layer-by-Layer Assembly of Cross-Functional Semi-transparent MXene-Carbon Nanotubes Composite Films for Next-Generation Electromagnetic Interference Shielding. Adv. Funct. Mater. 28, 1803360.

26. Zhou, Z., Liu, J., Zhang, X., Tian, D., Zhan, Z., and Lu, C. (2019). Ultrathin MXene/Calcium Alginate Aerogel Film for High-Performance Electromagnetic Interference Shielding. Adv. Mater. Interfac. 6, 1802040.

27. Jin, X., Wang, J., Dai, L., Liu, X., Li, L., Yang, Y., Cao, Y., Wang, W., Wu, H., and Guo, S. (2020). Flame-retardant poly(vinyl alcohol)/MXene multilayered films with outstanding electromagnetic interference shielding and thermal conductive performances. Chem. Eng. J. 380, 122475.

28. Zhao, S., Zhang, H.B., Luo, J.Q., Wang, Q.W., Xu, B., Hong, S., and Yu, Z.Z. (2018). Highly Electrically Conductive Three-Dimensional Ti$_3$C$_2$T$_x$ MXene/Reduced Graphene Oxide Hybrid Aerogels with Excellent Electromagnetic Interference Shielding Performances. ACS Nano 12, 11193–11202.

29. Bian, R., He, G., Zhi, W., Xiang, S., Wang, T., and Cai, D. (2019). Ultralight MXene-based aerogels with high electromagnetic interference shielding performance. J. Mater. Chem. C 7, 474–478.

30. Lu, X., Zhu, D., Li, X., and Wang, Y. (2022). Architectural design and interfacial engineering of CNTs@ZnIn$_2$S$_4$ heterostructure/cellulose aerogel for efficient electromagnetic wave absorption. Carbon 197, 209–217.

31. Wang, G., Liu, J., Liu, X., Li, M., Liu, J., Chai, N., Ye, F., Xue, J., Fan, X., Xu, H., et al. (2023). Oxidation-resistant vitamin C/MXene foam via surface hydrogen bonding for stable electromagnetic interference shielding in air ambient. Appl. Surf. Sci. 610, 155396.

32. Huang, S., and Mochalin, V.N. (2019). Hydrolysis of 2D Transition-Metal Carbides (MXenes) in Colloidal Solutions. Inorg. Chem. 58, 1958–1966.

33. Chae, Y., Kim, S.J., Cho, S.Y., Choi, J., Maleski, K., Lee, B.J., Jung, H.T., Gogotsi, Y., Lee, Y., and Ahn, C.W. (2019). An investigation into the factors governing the oxidation of two-dimensional Ti$_3$C$_2$ MXene. Nanoscale 11, 8387–8393.

34. Wyatt, B.C., Rosenkranz, A., and Anasori, B. (2021). 2D MXenes: Tunable Mechanical and Tribological Properties. Adv. Mater. 33, 2007973.

35. Zhao, X., Vashisth, A., Prehn, E., Sun, W., Shah, S.A., Habib, T., Chen, Y., Tan, Z., Lutkenhaus, J.L., Radovic, M., and Green, M.J. (2019). Antioxidants Unlock Shelf-Stable Ti$_3$C$_2$T$_x$ (MXene) Nanosheet Dispersions. Matter 1, 513–526.

36. Choi, E., Lee, J., Kim, Y.J., Kim, H., Kim, M., Hong, J., Kang, Y.C., Koo, C.M., Kim, D.W., and Kim, S.J. (2022). Enhanced stability of Ti$_3$C$_2$T$_x$ MXene enabled by continuous ZIF-8 coating. Carbon 191, 593–599.

37. Sreedhar, A., and Noh, J.S. (2021). Recent advances in partially and completely derived 2D Ti$_3$C$_2$ MXene based TiO$_2$ nanocomposites towards photocatalytic applications: A review. Sol. Energy 222, 48–73.

38. Iqbal, A., Hong, J., Ko, T.Y., and Koo, C.M. (2021). Improving oxidation stability of 2D MXenes: synthesis, storage media, and conditions. Nano Converg. 8, 9–22.

39. Natu, V., Hart, J.L., Sokol, M., Chiang, H., Taheri, M.L., and Barsoum, M.W. (2019). Edge Capping of 2D-MXene Sheets To Mitigate Oxidation in Aqueous Colloidal Suspensions. Angew. Chem. Int. Ed. Engl. 58, 12655–12660.

40. Berra, B., and Rizzo, A.M. (2009). Melatonin: circadian rhythm regulator, chronobiotic, antioxidant and beyond. Clin. Dermatol. 27, 202–209.

41. Zahedi, S.M., Hosseini, M.S., Abadía, J., and Marjani, M. (2020). Melatonin foliar sprays elicit salinity stress tolerance and enhance fruit yield and quality in strawberry (Fragaria x ananassa Duch.). Plant Physiol. Biochem. 149, 313–323.

42. Grzesik, M., Naparło, K., Bartosz, G., and Sadowska-Bartosz, I. (2018). Antioxidant properties of catechins: Comparison with other antioxidants. Food Chem. 241, 480–492.

43. Hu, Q., Li, G., Liu, X., Zhu, B., Chai, X., Zhang, Q., Liu, J., and He, C. (2019). Superhydrophilic Phytic-Acid-Doped Conductive Hydrogels as Metal-Free and Binder-Free Electrocatalysts for Efficient Water Oxidation. Angew. Chem. 58, 4318–4322.

44. Liu, L., Bashir, T., Abdalla, A.A., Salman, A., Ramos-Meza, C.S., Jain, V., Shabbir, M.S., and Yu, Z. (2022). Super-Tough and Environmentally Stable Aramid Nanofiber@MXene Coaxial Fibers with Outstanding Electromagnetic Interference Shielding Efficiency. Nano-Micro Lett. 14, 1–13.

45. Li, X., Wang, G., Li, Q., Wang, Y., and Lu, X. (2023). Dual optimized Ti$_3$C$_2$T$_x$

MXene@ZnIn$_2$S$_4$ heterostructure based on interface and vacancy engineering for improving electromagnetic absorption. Chem. Eng. J. *453*, 139488.

46. Li, Y., Yin, Z., Ji, G., Liang, Z., Xue, Y., Guo, Y., Tian, J., Wang, X., and Cui, H. (2019). 2D/2D/2D heterojunction of Ti$_3$C$_2$ MXene/MoS$_2$ nanosheets/TiO$_2$ nanosheets with exposed (001) facets toward enhanced photocatalytic hydrogen production activity. Appl. Catal., B *246*, 12–20.

47. Wang, H., Peng, R., Hood, Z.D., Naguib, M., Adhikari, S.P., and Wu, Z. (2016). Titania Composites with 2D Transition Metal Carbides as Photocatalysts for Hydrogen Production under Visible-Light Irradiation. ChemSusChem *9*, 1490–1497.

48. Xu, Y., Wang, S., Yang, J., Han, B., Nie, R., Wang, J., Wang, J., and Jing, H. (2018). In-situ grown nanocrystal TiO$_2$ on 2D Ti$_3$C$_2$ nanosheets for artificial photosynthesis of chemical fuels. Nano Energy *51*, 442–450.

49. Yang, C., Tang, Y., Tian, Y., Luo, Y., Faraz Ud Din, M., Yin, X., and Que, W. (2018). Flexible Nitrogen-Doped 2D Titanium Carbides (MXene) Films Constructed by an Ex Situ Solvothermal Method with Extraordinary Volumetric Capacitance. Adv. Energy Mater. *8*, 1802087.

50. Huang, H., Zhang, Z., Huang, D., Chen, D., Xu, Q., Li, H., He, J., and Lu, J. (2019). One-step in-situ preparation of N-doped TiO$_2$@C derived from Ti$_3$C$_2$ MXene for enhanced visible-light driven photodegradation. Appl. Catal. B *12*, 154–163.

51. Persson, I., Halim, J., Lind, H., Hansen, T.W., Wagner, J.B., Näslund, L.Å., Darakchieva, V., Palisaitis, J., Rosen, J., and Persson, P.O.Å. (2019). 2D Transition Metal Carbides (MXenes) for Carbon Capture. Adv. Mater. *31*, 1805472.

52. Hou, T., Li, Q., Zhang, Y., Zhu, W., Yu, K., Wang, S., Xu, Q., Liang, S., and Wang, L. (2020). Near-infrared light-driven photofixation of nitrogen over Ti$_3$C$_2$T$_x$/TiO$_2$ hybrid structures with superior activity and stability. Appl. Catal. B *273*, 119072.

53. Gao, W., Li, X., Luo, S., Luo, Z., Zhang, X., Huang, R., and Luo, M. (2021). In situ modification of cobalt on MXene/TiO$_2$ as composite photocatalyst for efficient nitrogen fixation. J. Colloid Interface Sci. *585*, 20–29.

54. Yun, T., Kim, H., Iqbal, A., Cho, Y.S., Lee, G.S., Kim, M.K., Kim, S.O., Kim, D., Gogotsi, Y., Kim, S.J., and Koo, C.M. (2020). Electromagnetic Shielding of Monolayer MXene Assemblies. Adv. Mater. *32*, 1906769.

55. Wan, Y.J., Rajavel, K., Li, X.M., Wang, X.Y., Liao, S.Y., Lin, Z.Q., Zhu, P.L., Sun, R., and Wong, C.P. (2021). Electromagnetic interference shielding of Ti$_3$C$_2$T$_x$ MXene modified by ionic liquid for high chemical stability and excellent mechanical strength. Chem. Eng. J. *408*, 127303.

56. Zhao, N., Hu, Y., Du, J., Liu, G., Dong, B., Yang, Y., Peng, J., Li, J., and Zhai, M. (2020). Ti$_3$C$_2$T$_x$ MXene-derived amorphous TiO$_2$-C nanosheet cocatalysts coupled CdS nanostructures for enhanced photocatalytic hydrogen evolution. Appl. Surf. Sci. *530*, 147247.

57. Zhang, C.J., Pinilla, S., McEvoy, N., Cullen, C.P., Anasori, B., Long, E., Park, S.H., Seral-Ascaso, A., Shmeliov, A., Krishnan, D., et al. (2017). Oxidation Stability of Colloidal Two-Dimensional Titanium Carbides (MXenes). Chem. Mater. *29*, 4848–4856.

58. Zhao, X., Holta, D.E., Tan, Z., Oh, J.H., Echols, I.J., Anas, M., Cao, H., Lutkenhaus, J.L., Radovic, M., and Green, M.J. (2020). Annealed Ti$_3$C$_2$T$_x$ MXene Films for Oxidation-Resistant Functional Coatings. ACS Appl. Nano Mater. *3*, 10578–10585.

59. Habib, T., Zhao, X., Shah, S.A., Chen, Y., Sun, W., An, H., Lutkenhaus, J.L., Radovic, M., and Green, M.J. (2019). Oxidation stability of Ti3C2Tx MXene nanosheets in solvents and composite films. NPJ 2D Mater. Appl. *3*, 8.

60. Che, R., Peng, L.M., Duan, X., Chen, Q., and Liang, X. (2004). Microwave absorption enhancement and complex permittivity and permeability of Fe encapsulated within carbon nanotubes. Adv. Mater. *16*, 401–405.

61. Sun, H., Che, R., You, X., Jiang, Y., Yang, Z., Deng, J., Qiu, L., and Peng, H. (2014). Cross-stacking aligned carbon-nanotube films to tune microwave absorption frequencies and increase absorption intensities. Adv. Mater. *26*, 8120–8125.

62. Liu, Q., Cao, Q., Bi, H., Liang, C., Yuan, K., She, W., Yang, Y., and Che, R. (2016). CoNi@SiO$_2$@TiO$_2$ and CoNi@Air@TiO$_2$ microspheres with strong wideband microwave absorption. Adv. Mater. *28*, 486–490.

63. Kong, L., Zhang, S., Liu, Y., Wu, H., Fan, X., Cao, Y., and Huang, J. (2023). Hierarchical architecture bioinspired CNTs/CNF electromagnetic wave absorbing materials. Carbon *207*, 198–206.

64. Che, R.C., Zhi, C.Y., Liang, C.Y., and Zhou, X.G. (2006). Fabrication and microwave absorption of carbon nanotubes/CoFe$_2$O$_4$ spinel nanocomposite. Appl. Phys. Lett. *88*, 033105.

65. Li, Z., Feng, D., Li, B., Xie, D., and Mei, Y. (2023). FDM printed MXene/MnFe$_2$O$_4$/MWCNTs reinforced TPU composites with 3D Voronoi structure for sensor and electromagnetic shielding applications. Compos. Sci. Technol. *231*, 109803.

66. Huang, H.D., Liu, C.Y., Zhou, D., Jiang, X., Zhong, G.J., Yan, D.X., and Li, Z.M. (2015). Cellulose composite aerogel for highly efficient electromagnetic interference shielding. J. Mater. Chem. A. *3*, 4983–4991.

67. Lencar, C.C., Ramakrishnan, S., and Sundararaj, U. (2022). Carbon Nanotube Migration in Melt-Compounded PEO/PE Blends and Its Impact on Electrical and Rheological Properties. Nanomaterials *12*, 3772.

68. Yan, A., Liu, Y., Wu, Z., Gan, X., Li, F., Tao, J., Li, C., and Yi, J. (2022). RGO reinforced Cu foam with enhanced mechanical and electromagnetic shielding properties. J. Mater. Res. Technol. *21*, 2965–2975.

69. Xia, B., Zhang, X., Jiang, J., Wang, Y., Li, T., Wang, Z., Chen, M., Liu, T., and Dong, W. (2022). Facile preparation of high strength, lightweight and thermal insulation Polyetherimide/Ti$_3$C$_2$T$_x$ MXenes/Ag nanoparticles composite foams for electromagnetic interference shielding. Compos. Commun. *29*, 101028.

70. Xiang, C., Guo, R., Lin, S., Jiang, S., Lan, J., Wang, C., Cui, C., Xiao, H., and Zhang, Y. (2019). Lightweight and ultrathin TiO$_2$-Ti$_3$C$_2$T$_x$/graphene film with electromagnetic interference shielding. Chem. Eng. J. *360*, 1158–1166.

71. Xu, H., Yin, X., Li, X., Li, M., Liang, S., Zhang, L., and Cheng, L. (2019). Lightweight Ti$_2$CT$_x$ MXene/Poly(vinyl alcohol) Composite Foams for Electromagnetic Wave Shielding with Absorption-Dominated Feature. ACS Appl. Mater. Interfaces *11*, 10198–10207.

72. Xu, J., Li, R., Ji, S., Zhao, B., Cui, T., Tan, X., Gou, G., Jian, J., Xu, H., Qiao, Y., et al. (2021). Multifunctional Graphene Microstructures Inspired by Honeycomb for Ultrahigh Performance Electromagnetic Interference Shielding and Wearable Applications. ACS Nano *15*, 8907–8918.

73. Wu, Z., Pei, K., Xing, L., Yu, X., You, W., and Che, R. (2019). Enhanced microwave absorption performance from magnetic coupling of magnetic nanoparticles suspended within hierarchically tubular composite. Adv. Funct. Mater. *29*, 1901448.

STAR★METHODS

KEY RESOURCES TABLE

REAGENT or RESOURCE	SOURCE	IDENTIFIER
Biological samples		
Lithium fluoride (LiF, ≥99%)	Aladdin Biochemical Polytron Technologies	CAS:7789-24-4
Hydrochloric acid solution (HCl, 37 wt.%)	Aladdin Biochemical Polytron Technologies	CAS:7647-01-0
Melatonin	Aladdin Biochemical Polytron Technologies	CAS:73-31-4
Tea polyphenols	Aladdin Biochemical Polytron Technologies	CAS:84650-60-2
Phytic acid	Aladdin Biochemical Polytron Technologies	CAS:83-86-3
Ti_3AlC_2 (≥98% purity)	Beijing Lianlixin Technology	CAS:196506-01-1
Deposited data		
All data reported in this paper will be shared by the lead contact upon request.		

RESOURCE AVAILABILITY

Lead contact

Further information and requests for resources and reagents should be directed to and will be fulfilled by the lead contact, Xingmin Liu (liuxingmin19890101@126.com).

Materials availability

This study did not generate new unique reagents.

Data and code availability

- All data reported in this paper will be shared by the lead contact upon request.

- This paper does not report original code.

- Any additional information required to reanalyze the data reported in this paper is available from the lead contact upon request.

METHOD DETAILS

Materials

Lithium fluoride (LiF, ≥99%), hydrochloric acid solution (HCl, 37 wt.%), melatonin, tea polyphenols, and phytic acid were purchased from Aladdin Biochemical Polytron Technologies, Inc. Ti_3AlC_2 (≥98% purity) powders were purchased from Beijing Lianlixin Technology Co., Ltd., China. No further purification of the chemicals was implemented before the experiments.

Synthesis of few-layered $Ti_3C_2T_x$ MXene flakes

For the preparation of few-layered $Ti_3C_2T_x$ MXene, 1.6 g of LiF was dissolved in 20 ml of HCl (8 M) with the assistance of magnetic stiring force. After 30 min, 1 g of Ti_3AlC_2 powder was slowly emerged into the LiF-HCl solution while maintaining at 40°C to allow for the etching of Al elements from the MAX phase and exfoliation of the MXene flakes. After 24 h, the suspension was centrifuged at 3500 r/min for 5 min. The sediments from the centrifugation were discarded. The suspension from the first cycle of centrifugation was then further centrifuged at a higher speed (10000 r/min). After 7 min, the MXene powdere were collected and washed 5 times with deionized water (DI). Finally, the few-layered $Ti_3C_2T_x$ powders were freeze-dried.

Preparation of $Ti_3C_2T_x$/antioxidant and $Ti_3C_2T_x$ foam composites

To start with, the freeze-dried $Ti_3C_2T_x$ MXene powders were dispersed in deionized water to form a stable dispersion with a concentration of 30 mg/ml. Antioxidants (i.g., melatonin, tea polyphenols, and phytic acid) with different mass fractions to MXene (i.g., 16 wt.%, 20 wt.%, 25 wt.%, and 33 wt.%) were then dissolved into the MXene dispersion. After stirring for 30 minutes, the resulting dispersions were poured

into three rectangular molds with dimensions of $33.0 \times 20.0 \times 2.0$ mm^3 and immediately frozen with liquid nitrogen. Finally, the samples were freeze-dried and cut into samples with a size of $22.9 \times 10.2 \times 2.0$ mm^3 for EM measurements. Based on the name of the antioxidants, the composite materials were named as $Ti_3C_2T_x$/MLT, $Ti_3C_2T_x$/TP and $Ti_3C_2T_x$/PA. For the composites with identical ingredients while containing-different antioxidant content, they are differentiated by their mass ratios. For example, 20%-$Ti_3C_2T_x$/MLT means that the MLT content is 20 wt.% of the $Ti_3C_2T_x$/MLT composite material. Meanwhile, $Ti_3C_2T_x$ foams without antioxidants were also prepared as control test samples.

Materials characterization

Scanning electron microscopy (SEM) (Hitachi, S-4700, 15 kV) was employed to characterize the morphology of foam composites before and after exposing to air. The crystalline lattice of the MXene in the composites was confirmed with transmission electron microscopy (TEM) (FEI Tecnai, F200X, 200 kV). X-ray diffraction (XRD) (X'Pert Pro, Philips, Netherlands, Cu Kα radiation) was employed to obtain the phase crystallinity. XPS (Axis Supra, Kratos, UK) was employed to characterize the bonding and element information of MXene-based materials. Raman spectra were recorded via a micro-Raman HR8000 spectrometer (Bensheim, Horiba Jobin Yvon, Germany, 514.5 nm) to obtain the crystallinity of the carbon phase. The compression test was performed using a computerized universal material testing machine (HZ-10048, 50 N), and the size of the tested sample was $22.9 \times 10.2 \times 2.0$ mm^3.

Measurement of EMI shielding performance

A vector network analyzer (VNA, Agilent Technologies E8362B) was used to characterize the S-parameters of foam composites in the X-band (8.2 to 12.4 GHz). $Ti_3C_2T_x$ foam and $Ti_3C_2T_x$/antioxidant foam composites were cut into rectangular monoliths with 3 dimensions of $22.9 \times 10.2 \times 2.0$ mm^3. The EMI SE is defined as the logarithmic ratio of incident power to transmission power. The total SE (SE_T) is the sum of reflection shielding effectiveness (SE_R), absorption shielding effectiveness (SE_A), and multiple reflection shielding effectiveness (SE_{MR}).[60,70–72] SE_{MR} can be ignored when SE is larger than 10 dB. Scattering parameters (S11, S12, S21, and S22) were obtained directly from VNA and used to calculate SE_T, SE_A, and SE_R according to the following equations.[61–64,73]

$$SE_T = 10 \log\left(\frac{1}{|S_{21}|^2}\right) \qquad \text{(Equation 1)}$$

$$SE_R = 10 \log\left(\frac{1}{1 - |S_{11}|^2}\right) \qquad \text{(Equation 2)}$$

$$SE_A = 10 \log\left(\frac{1 - |S_{11}|^2}{|S_{21}|^2}\right) \qquad \text{(Equation 3)}$$

The absorption (A), reflection (R), and transmission (T) coefficients were calculated as:

$$T = |S_{12}|^2 = |S_{21}|^2 \qquad \text{(Equation 4)}$$

$$R = |S_{11}|^2 = |S_{22}|^2 \qquad \text{(Equation 5)}$$

$$A + R + T = 1 \qquad \text{(Equation 6)}$$